International Journal of Hydrogen Energy

Exploration of 1D-2D Nanocomposite via Coupling of LaFeO3 with Reduced Graphene Oxide for Photocatalytic Water Splitting
--Manuscript Draft--

Abstract:	Sustainable energy innovation is spearheading the way to achieve decarbonisation through commercially viable and highly competitive renewable technologies for green hydrogen. Photocatalytic water splitting has received global attention, as it promotes the direct conversion of solar energy to chemical energy and hydrogen production. Lanthanum orthoferrite (LaFeO3) has been selected due to its narrow bandgap perovskite-oxides (ABO3) type nature, low cost and high chemical stability but it is limited with fast charge recombination. To circumvent its constraint of fast charge recombination, an efficient graphene-based nanocomposite has been prepared by employing reduced graphene oxide (RGO) nanosheets as charge separators for visible light driven photocatalytic water splitting. Here, we present a thorough physical and spectroscopic characterization of the Lanthanum orthoferrite/Reduced Graphene oxide (LaFeO3/RGO) nanocomposites, and investigate its photocatalytic and photoelectrochemical performance. The photocurrent density of the nanocomposites demonstrated ~21 times higher in comparison to pure LaFeO3. The as-prepared nanocomposites have been successfully used as photocatalysts for H2 generation through water reduction under visible light. A significant enhancement in H2 generation has been recorded for nanocomposites (~82 mmol g−1 h−1) as compared to that of bare LaFeO3 (~9 mmol g−1 h−1) which is among the highest values obtained using noble-metal-free graphene-based photocatalytic nanocomposites. This work offers a facile approach for fabricating highly efficient 1D-2D heterostructure for photocatalysis application.

Exploration of 1D-2D Nanocomposite via Coupling of LaFeO$_3$ with Reduced Graphene Oxide for Photocatalytic Water Splitting

Soumita Samajdar[1,2], Susmita Bera[1], Pradip Sekhar Das[1], Harry Finch[3], Vinod R. Dhanak[3], Saswata Chakraborty[2,4], T. Maiyalagan[5], K. Annapurna[2,4], Srabanti Ghosh[*1,2]

[1]*Energy Materials & Devices Division, CSIR - Central Glass and Ceramic Research Institute Raja S. C. Mullick Road, Jadavpur, Kolkata-700032, India*
[2]*Academy of Scientific & Innovative Research (AcSIR), Ghaziabad, India*
[3]*Stephenson Institute for Renewable Energy and Department of Physics, University of Liverpool, Liverpool L69 7ZF, United Kingdom*
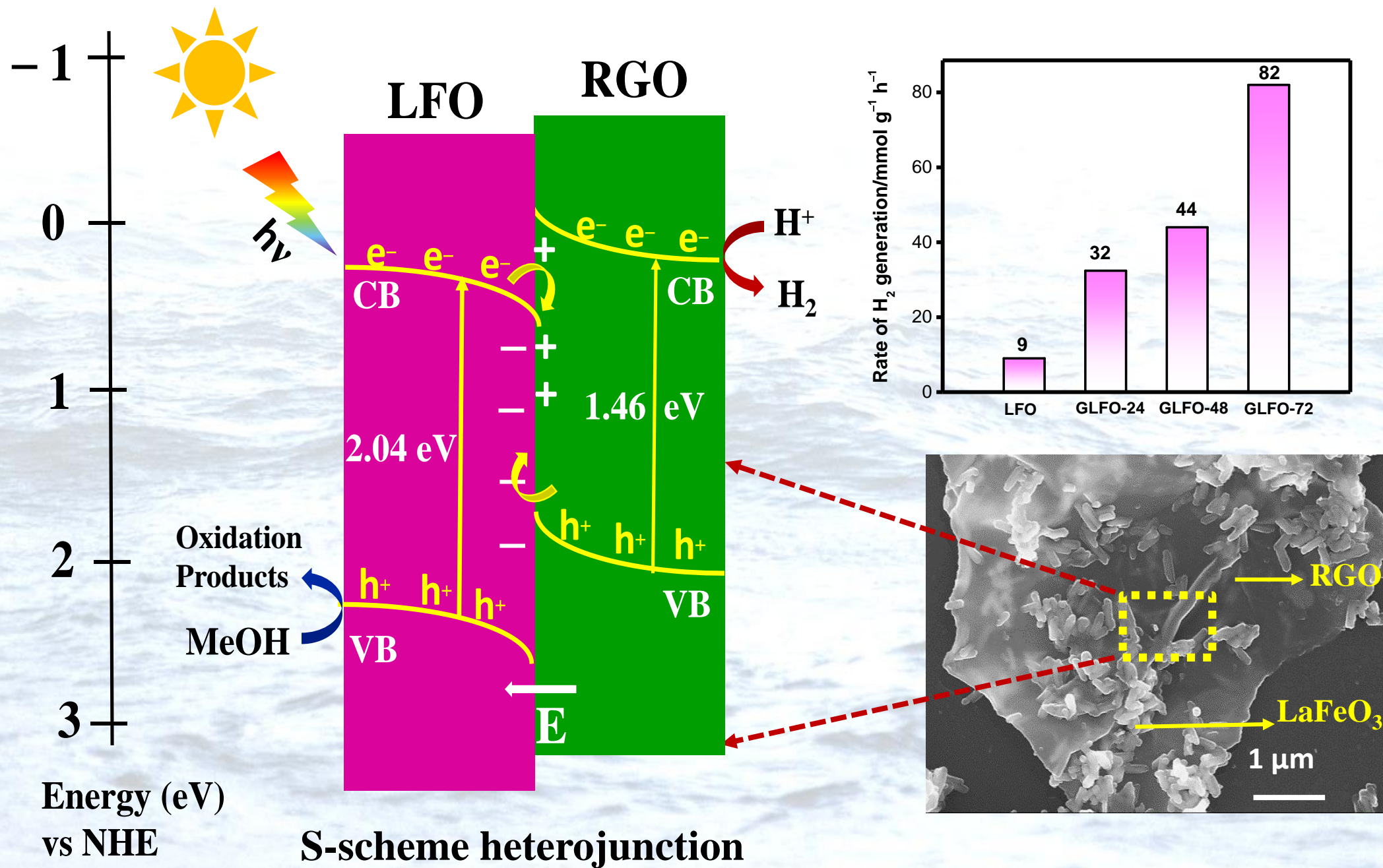[4]*Specialty Glass Division, CSIR - Central Glass and Ceramic Research Institute Raja S. C. Mullick Road, Jadavpur, Kolkata-700032, India*
[5]*Department of Chemistry, Faculty of Science and Humanities, SRM Institute of Science and Technology, Kattankulathur, India*

*Email: srabanti@cgcri.res.in

Highlights (for review)

• An efficient 1D-2D heterostructures were prepared via facile hydrothermal method.

• LaFeO$_3$/RGO exhibited high photocatalytic activity for H$_2$ production.

• LaFeO$_3$/RGO showed excellent photoelectrochemical response.

• S scheme band alignment was proposed for better photocatalytic activity.

S-scheme heterojunction

Exploration of 1D-2D Nanocomposite via Coupling of LaFeO₃ with Reduced Graphene Oxide for Photocatalytic Water Splitting

Soumita Samajdar[1,2], Susmita Bera[1], Pradip Sekhar Das[1], Harry Finch[3], Vinod R. Dhanak[3], Saswata Chakraborty[2,4], T. Maiyalagan[5], K. Annapurna[2,4], Srabanti Ghosh[*1,2]

[1]*Energy Materials & Devices Division, CSIR - Central Glass and Ceramic Research Institute Raja S. C. Mullick Road, Jadavpur, Kolkata-700032, India*
[2]*Academy of Scientific & Innovative Research (AcSIR), Ghaziabad, India*
[3]*Stephenson Institute for Renewable Energy and Department of Physics, University of Liverpool, Liverpool L69 7ZF, United Kingdom*
[4]*Specialty Glass Division, CSIR - Central Glass and Ceramic Research Institute Raja S. C. Mullick Road, Jadavpur, Kolkata-700032, India*
[5]*Department of Chemistry, Faculty of Science and Humanities, SRM Institute of Science and Technology, Kattankulathur, India*

*Email: srabanti@cgcri.res.in

ABSTRACT

Sustainable energy innovation is spearheading the way to achieve decarbonisation through commercially viable and highly competitive renewable technologies for green hydrogen. Photocatalytic water splitting has received global attention, as it promotes the direct conversion of solar energy to chemical energy and hydrogen production. Lanthanum orthoferrite (LaFeO₃) has been selected due to its narrow bandgap perovskite-oxides (ABO₃) type nature, low cost and high chemical stability but it is limited with fast charge recombination. To circumvent its constraint of fast charge recombination, an efficient graphene-based nanocomposite has been prepared by employing reduced graphene oxide (RGO) nanosheets as charge separators for visible light driven photocatalytic water splitting. Here, we present a thorough physical and spectroscopic characterization of the Lanthanum orthoferrite/Reduced Graphene oxide (LaFeO₃/RGO) nanocomposites, and investigate its photocatalytic and photoelectrochemical performance. The photocurrent density of the nanocomposites demonstrated ~21 times higher in comparison to pure LaFeO₃. The as-prepared nanocomposites have been successfully used as photocatalysts for H_2 generation through water reduction under visible light. A significant enhancement in H_2 generation has been recorded for nanocomposites (~82 mmol g^{-1} h^{-1}) as compared to that of bare LaFeO₃ (~9 mmol g^{-1} h^{-1}) which is among the highest values obtained using noble-metal-free graphene-based photocatalytic nanocomposites. This work offers a facile approach for fabricating highly efficient 1D-2D heterostructure for photocatalysis application.

Keywords: Reduced Graphene oxide nanosheets, Lanthanum orthoferrite, Nanocomposites, Photocatalytic H_2 generation, Photoelectrochemical properties

INTRODUCTION

Developing a sustainable energy future is one of the biggest challenges in the 21st century, energy conversion technologies such as solar energy harvesting play a vital role in the transition to a renewable energy system. As solar energy is a decentralized and inexhaustible natural resource, solar energy harvesting offers a desirable approach for realization of sustainable future energy supply under minimal environmental impact [1−3]. Photocatalytic water splitting has received global attention, as it is an eco-friendly and sustainable approach for low-cost and green H_2 production [4−6]. Fujishima and Honda (1972) first reported photoelectrochemical water splitting using a titanium dioxide (TiO_2) photoanode which is the most well explored catalyst due to its high stability, non-toxicity and cost-effectiveness [7]. Nevertheless, the applications of TiO_2 are limited because of a low quantum yield and fast charge carriers recombination [8−10]. Besides TiO_2, other metal oxides like WO_3, SnO_2, ZnO etc. have also been used as photocatalysts, but their applications are also limited as they are wide bandgap semiconductors, which are capable of absorbing only UV irradiation [11].

As an alternative to traditional metal oxide semiconductors, perovskite based oxide materials have stimulated an ever-increasing interest in solar to chemical energy conversion applications [12]. Perovskite oxides are highly crystalline and stable materials with special ABO_3 structure which show an advantage over other semiconductor photocatalysts due to their high thermal stability, structural tunability, high electronic conductivity, excellent charge carrier mobilities and high absorbance coefficients and narrow band gaps which makes them capable of solar light absorption in the visible region [13−15]. Among various perovskites, lanthanum ferrite ($LaFeO_3$) has received great importance in the field of photocatalysis due to their narrow band gap, high stability and non-toxicity, however, restricted with fast charge carrier recombination [16]. Moreover, the positive conduction band potential of bare $LaFeO_3$ does not make it ideal for H_2 generation [17]. In order to overcome these limitations, various strategies, such as the

formation of heterostructures with different dimensional interfaces such as 0D-2D, 1D-2D, 2D-2D etc. via combination with suitable semiconductors have been developed which may hinder the fast charge-carrier recombination [18–21]. The 1D-2D interface enables rapid and long-distance transport of electrons along the longitudinal dimensions which promotes facile charge separation along the 1D nanostructures. It also mitigates the disadvantages of the low surface area of the 1D nanostructures and prevents the restacking of the 2D nanosheets, which leads to the enhancement in photocatalytic efficiency [22–27]. Recently, our group has designed 1D-2D heterostructures of $CuFe_2O_4$/BiOCl which demonstrated 5.7 times higher rate of H_2 generation than pure BiOCl due to the formation of the direct Z-scheme heterostructure promoting facile charge transfer and charge separation [25]. Bera et al. [26] fabricated highly active heterostructured photocatalyst composed of Ag nanoparticles decorated $AgVO_3$ nanorods and 2D MoS_2 nanosheets that exhibited 20 times higher rate of H_2 generation as compared to bare MoS_2. Notably, the Z-scheme interfacial charge-transfer mechanism may facilitate the charge separation and lowers the rate of electron-hole recombination. In another example, 1D-2D heterojunction of CdS nanorods and TiO_2 nanosheets displayed 3.7 times higher rate of hydrogen generation as compared to P25 TiO_2/CdS composites which may be due to higher photogenerated charge separation and superior electron transfer ability [27].

Remarkably, graphene based 2D materials have been widely used in the field of photocatalysis due to their fascinating properties such as visible light absorption, superior electron mobility, high conductivity, large surface area and cost-effectiveness [28–30]. In order to overcome the fast charge-carrier recombination rate of metal oxide photocatalyst, it may be combined with reduced graphene oxide nanosheets (RGO) which improves the photocatalytic performance of metal oxide. For example, Dang et al. [31] fabricated titanate nanotube/graphene 1D-2D nanocomposites which exhibited three times enhancement in photocatalytic H_2 generation rate as compared to bare titanates. The incorporation of RGO to the titania nanotubes effectively

lowers the rate of electron-hole recombination which in turn increases the photocatalytic efficiency of the nanocomposites. Alsulami et al. [32] achieved a significantly high rate of photocatalytic H_2 generation of ~2100.4 µmol h^{-1} g^{-1} using RGO/FeVO$_4$ 2D-1D nanocomposites which shows enhanced visible light absorption and facilitates the separation of the photogenerated charge carriers of FeVO$_4$ in presence of RGO. Hafeez et al. [33] also reported a ternary InVO$_4$-g-C$_3$N$_4$/RGO hybrid nanocomposites exhibited a superior rate of hydrogen production of ~7449 µmol h^{-1} g^{-1}. There are limited reports available in the literature regarding the use of LaFeO$_3$/RGO nanocomposites for photocatalytic H_2 generation. For example, Acharya et al. [34] reported 2.5 times enhancement in the rate of hydrogen generation by photocatalytic water splitting for 2D-3D nanocomposites of LaFeO$_3$ nanospheres/RGO composite as compared to LaFeO$_3$. The formation of the nanocomposites decreases the rate of electron–hole recombination and enhances visible-light absorption. Orak et al. [35] reported that the 2D-3D nanocomposites of Graphene-supported LaFeO$_3$ catalyst is 2.9 times more active than LaFeO$_3$ towards visible-light driven photocatalytic hydrogen generation from sucrose solution under similar test conditions. The introduction of reduced graphene oxide lowers the band gap and increases the surface area, which provides abundant active sites. However, there has been limited study regarding the photoelectrochemical properties of the nanocomposites and the charge-transfer mechanism, which occurs at the interface of the two semiconductors and this needs to be explored further. To the best of our knowledge, the impact of RGO in photo-electrochemical response and catalytic activity of LaFeO$_3$ nanorods has not yet been investigated.

The present work describes fabrication of a two-dimensional (2D) RGO with one dimensional (1D) LaFeO$_3$ nanorods to form nanocomposites *via* a facile hydrothermal method, which shows a significantly high rate of photocatalytic H_2 evolution. The structural, optical properties of bare LaFeO$_3$ and its nanocomposites have been studied in details. Furthermore,

photoelectrochemical measurements provide insights into the charge transport properties at the composite interface. The enhanced photo-response and photocatalytic H_2 generation of the nanocomposites have been explored on the basis of band structure and charge-transfer mechanism through formation of S-scheme heterojunction.

2. EXPERIMENTAL SECTION

2.1 Chemicals

Lanthanum nitrate hexahydrate ($La(NO_3)_3.6H_2O$) was obtained from Acros Organics. Iron nitrate nonahydrate ($Fe(NO_3)_3.9H_2O$) and potassium hydroxide were obtained from Merck. Polyethylene glycol was obtained from Fisher Chemicals. All experiments were performed at room temperature. DI water (18.2 MΩ.cm) was obtained from Millipore System.

2.2 Synthesis of LaFeO₃

LaFeO₃ was synthesized *via* a facile hydrothermal method followed by heat treatment. A 30 mL aqueous solution of 0.002 M $La(NO_3)_3.6H_2O$ was prepared in a beaker by stirring for 10 mins. Then, 10 mL aqueous solution of 0.004 M $Fe(NO_3)_3.9H_2O$, 10 mL aqueous solution of PEG (~ 1.6 g) and 25 mL aqueous 2M KOH solution were prepared in separate beakers. These solutions were then added dropwise into the $La(NO_3)_3$ solution under vigorous stirring condition. After 1h stirring, the resulting solution was transferred into a 100 mL capacity autoclave, and heated at 200°C for 72 h. The resulting sample was collected, washed and dried in an oven at 60°C. The final light violet powder of LaFeO₃ was obtained and marked as LFO.

2.3 Synthesis of LaFeO₃/Reduced Graphene Oxide (GLFO) nanocomposites

Graphene oxide (GO) have been synthesized by Modified Hummer's method [36]. A facile hydrothermal method has been developed to synthesize LaFeO$_3$/Reduced Graphene oxide (GLFO) nanocomposites. The process schematic is shown in Scheme 1. At first, GO (0.5 mg/mL) was dispersed in water and sonicated for 45 minutes. Then, 0.002 M La(NO$_3$)$_3$.6H$_2$O was added to the aqueous solution of GO. In separate beakers, 10 mL aqueous solution of 0.004 M Fe(NO$_3$)$_3$.9H$_2$O, 10 mL aqueous solution of PEG (~1.6 g) and 2M 25 mL aqueous KOH solution were prepared. These solutions were then added into La(NO$_3$)$_3$ solution dropwise under vigorous stirring. After magnetic stirring for 1 hour, the resulting solution was transferred into a 100 mL capacity autoclave, heated at 200°C for 72 h. After hydrothermal treatment at 200°C for 72 hrs, the black powder of the GLFO nanocomposites was centrifuged several times with distilled water and absolute ethanol, in order to remove the unreacted precursors. The resulting sample was collected and dried in an oven at 60°C to obtain the GLFO nanocomposites.
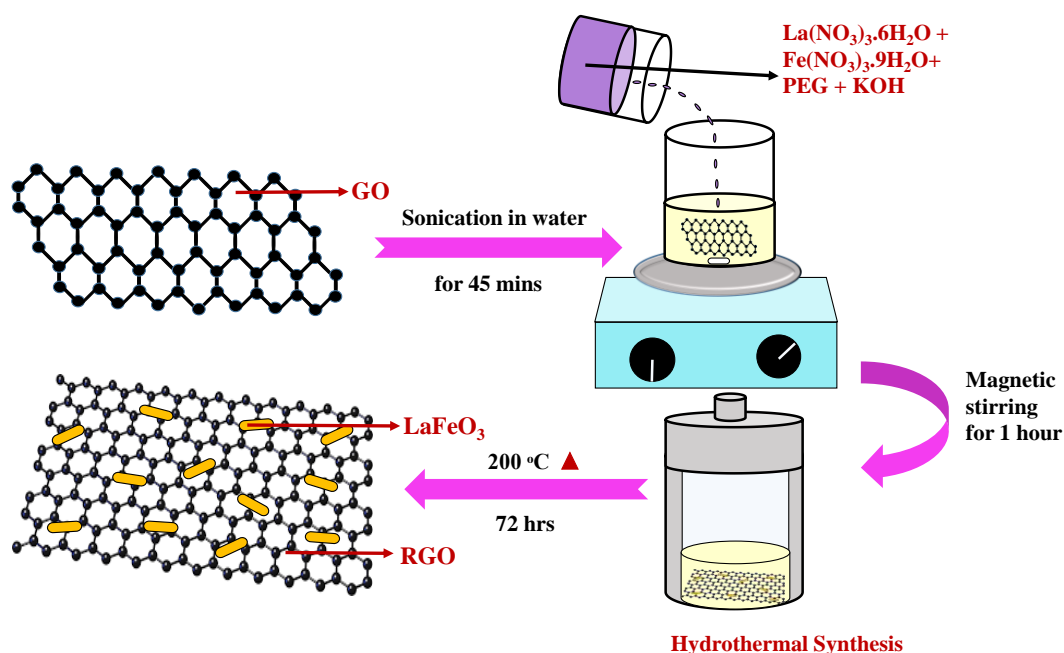
Scheme 1 − Synthesis scheme of LaFeO$_3$/Reduced Graphene oxide (GLFO) nanocomposites.

2.4 Characterization

The X-ray diffraction (XRD) patterns were recorded using a Philips X'Pert diffractometer (at a scan rate of $1°$ min^{-1}). Transmission electron microscopy (TEM, Tecnai G^2 30ST, FEI) operating at 300 kV, and scanning electron microscopy (SEM, Sigma, LEO. 430i, Carl-Zeiss) were used to determine the morphology of LFO and the composites. Thermo gravimetric analysis was performed using a NETZSCH, STA 449 F3, Jupiter under argon flow at a heating rate of $10°C$ min^{-1} (flow rate of 30 ml min^{-1} was used). The absorption properties and bandgap were examined using a UV–visible spectrophotometer (Shimadzu UV-3600 spectrophotometer) over a wavelength region of 300 to 800 nm. The N_2 adsorption-desorption isotherm was carried out by Quantachrome, FL-33426. FTIR analysis of the samples was performed using Thermo Nicolet 6700 spectrophotometer in the range from 400 to 4000 cm^{-1}. XPS was carried out to measure the core-level spectra, VB DoS, and secondary electron cutoff (SEC) of the as synthesized LFO and GLFO. Raman spectra of LFO and GLFO have been performed using a Micro Raman setup (Horiba LabRAM) with an excitation line of 532 nm.

2.5 Photoelectrochemical measurements. The photoelectrochemical properties of pure LFO and GLFO were studied by preparing thin films on FTO coated glass slides using three-electrode quartz cell and galvanostat-potentiostat (PGSTAT302 N, Autolab, The Netherlands) under 350W Xenon lamp.

The thin film of the materials was prepared by spin coating. For the spin-coating method, a LFO, GLFO solution was prepared as follows: LFO or GLFO powder was dispersed in absolute ethanol under sonication for 30 mins. After that, 3 layers of the solution (each layer containing 50 µL of the solution) were coated on the conducting side of the FTO glass.

The linear sweep voltammetry measurement was carried out within the potential range -0.2 V to 1.0 V vs Ag/AgCl at a scan rate 10 mV/s using 0.1 M Na_2SO_4 (pH 7) as electrolyte. The

2.6 Photocatalytic H₂ generation. Photocatalytic H_2 generation was tested in a closed quartz cell with catalyst (0.5 gm/L) under visible light irradiation (250 W Xenon lamp) through online gas chromatography (GC) using 15 vol% methanol as sacrificial agent.

3. RESULTS AND DISCUSSION

3.1 Phase purity and crystal structure

Powder XRD was performed in order to determine the crystalline phase of the as-synthesized nanocomposites. Fig. 1 shows the XRD patterns of pure LFO and GLFO nanocomposites synthesized for 72 hrs and calcined at a temperature of 500° C. The strong peaks at 2θ values correspond to characteristic diffraction from (112), (021), (120), (202), (113), (220), (213), (131), (204) and (133) planes of LaFeO₃ respectively, indicating the orthorhombic phase of pure LaFeO₃ with space group Pnma [JCPDS Card No: 01-070-7777] and lattice parameters a= 5.5594 Å , b = 7.8498 Å and c = 5.5509 Å. GLFO nanocomposites displayed strong peak at 2θ value of 25.9° correspond to the characteristic diffraction from the (002) plane of reduced graphene oxide nanosheets (RGO) [37, 38]. Therefore, XRD pattern of the GLFO nanocomposites showed the characteristic peaks of both orthorhombic phase of pure LFO and RGO, which indicates the successful formation of the nanocomposites.
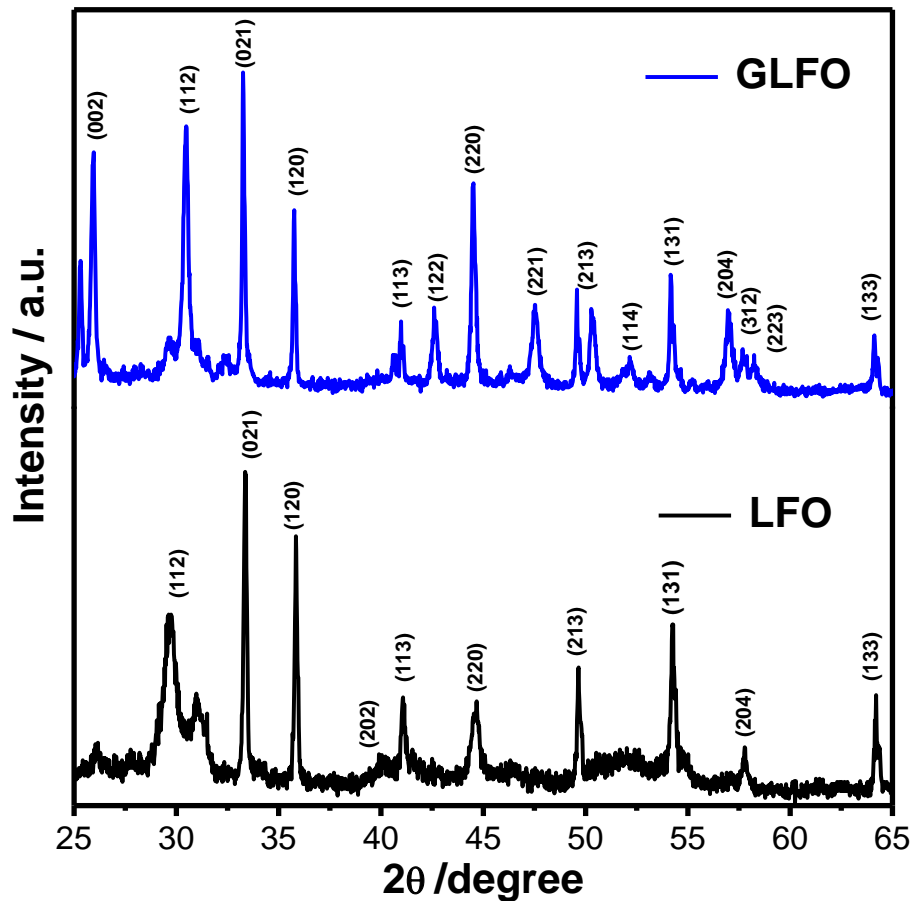
Fig. 1 – XRD Pattern of LFO and GLFO nanocomposites prepared at 72 hrs.

Fig. S1 shows the XRD patterns of the LFO and GLFO nanocomposites synthesized at 24 and 48 hrs respectively. The XRD pattern of the nanocomposites synthesized shows that no crystal phase formation occurs during 24 hrs growth time. In the XRD pattern of the nanocomposites synthesized at 48 hrs, many additional peaks, corresponding to the diffraction from the planes of other mixed oxides are present. Thus, 72 hrs are required for the successful formation of the nanocomposites.

3.2 Raman Spectra

Raman analysis was carried out both for LFO and GLFO (Fig. 2) to analyse the chemical nature. In the Raman spectrum of the GLFO nanocomposites, bands at 288 cm^{-1}, 346 cm^{-1}, 405 cm^{-1}, and 645 cm^{-1} correspond to the A_g, B_{1g}, B_{2g} and B_{3g} modes of pure LFO and the peaks at 1356 cm^{-1}, and 1595 cm^{-1} correspond to the D and G bands of RGO respectively [39–41]. After composite formation, the D band has been shifted to 1598.56 cm^{-1}, which clearly implies that the defect sites produced higher energy than pristine compound. The higher energy Raman peak corroborated the higher interaction between defective sites (hetero atom present in the graphitic unit such as oxygen) and LFO. Further, the Raman scattering of G band appears at 1352 cm^{-1} for GLFO composites, which is 3 cm^{-1} lower than the GO. The decrease in the Raman scattering band for GLFO indicated the weakly localized graphitic bond electrons than the GO, which could be attributed by the bond formation between Fe and oxygen, further confirmed by XPS analysis (Fig. 3c). The D/G intensity ratio may indicate the disorder or restoration of the graphene lattice, considering the sp^2/sp^3 carbon ratio [42]. The D/G intensity ratio for GO and GLFO nanocomposites are 0.85 and 0.96, respectively. The higher interaction between LFO and defective site heteroatoms may the reason behind slight increase in the D/G intensity ratio. In addition, the increase of D/G ratio indicates electron-donating nature of GO to LFO [43].
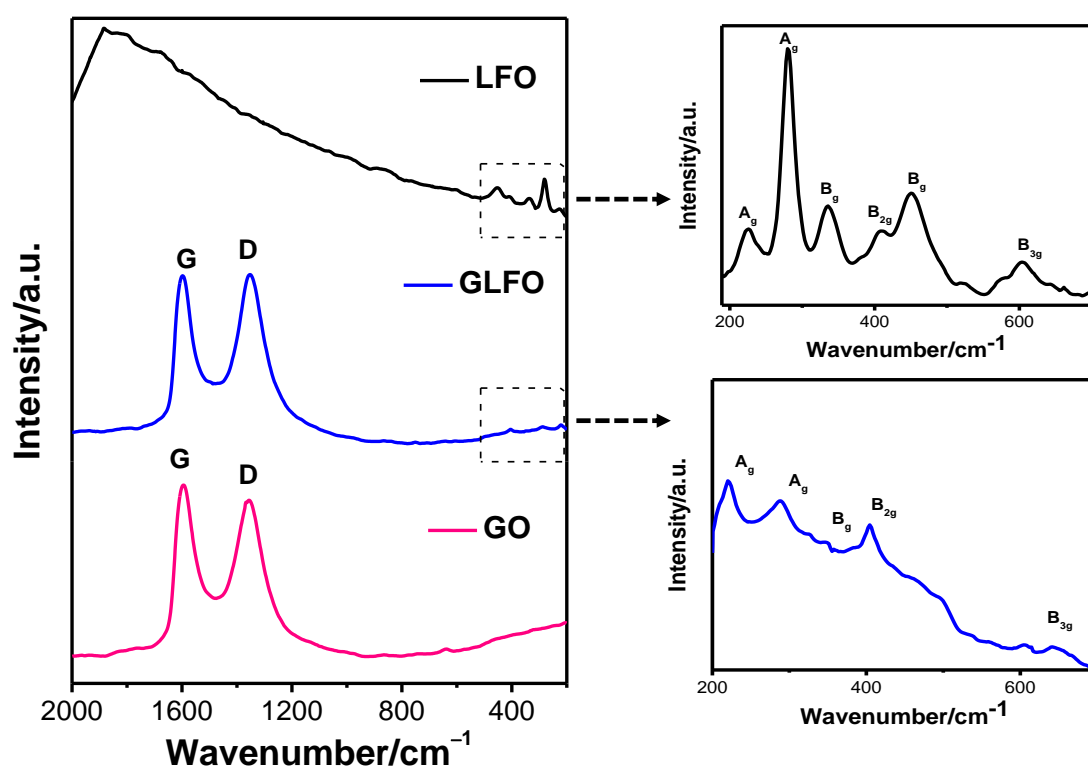
Fig. 2 – Raman spectra of GO, GLFO nanocomposites and bare LFO.

3.3 X-ray Photon Spectroscopy and surface composition

X-ray photon spectroscopy (XPS) was performed to elucidate the oxidation states and the chemical environment of the elements present in pure LFO and GLFO nanocomposites. The measurements were performed in a custom built ultra-high vacuum system consisting of a commercial SPECS monochromated Al-kα X-ray source and a PSP Vacuum Technology hemispherical electron energy analyser, operated with an overall energy resolution of ±0.1 eV. Fig. 3a shows the surface survey spectra of LFO and GLFO nanocomposites, which confirms the presence of La, Fe, O and C after composite formation. Fig. 3b shows the La 3d core levels for bare LFO and GLFO. The La $3d_{5/2}$ lineshape of LFO, fitted with two doublet peaks at the binding energies of ~839.57 eV and ~836.2 eV confirms the presence of La^{3+} state [35]. However, after composite formation, both the peaks have been shifted to lower binding

energies of ~837.5 eV and ~834.1 eV. Such a shift to the lower binding energy suggests the increase in electron density around La^{3+} due to transfer of electrons from RGO to LFO in the nanocomposite, which is well consistent with the Raman data (Fig. 2) and further confirmed by the energy diagram analysis (Fig. 9). Fig. 3c shows the Fe 2p core levels for bare LFO and GLFO nanocomposites. Two characteristic peaks in the Fe 2p lineshape at binding energies of ~709.8 eV and ~723.17 eV correspond to Fe $2p_{3/2}$ and Fe $2p_{1/2}$, respectively, and confirms the presence of Fe^{3+} state in LFO. After composite formation, the Fe peaks are not resolved properly. The O 1s lineshape for bare LFO has been fitted with three peaks at binding energies of ~528.3eV, ~529.9 eV and ~530.9 eV which corresponds to the lattice oxygens of La−O and Fe−O and surface adsorbed oxygen, respectively (Fig. 3d). After composite formation, the O1s peaks have been shifted to higher binding energies i.e. ~528.5 eV, ~530.5 eV and ~532.3 eV respectively [44]. The peak shifting is attributed mainly due to interaction of RGO with LFO, and further indicates the successful formation of nanocomposites. The two characteristic peaks in the C 1s spectrum at binding energies of ~ 284.4 eV and ~ 287.1 eV correspond to C−C and C−O bonds of RGO nanosheets, respectively (Fig. 3e) [45].
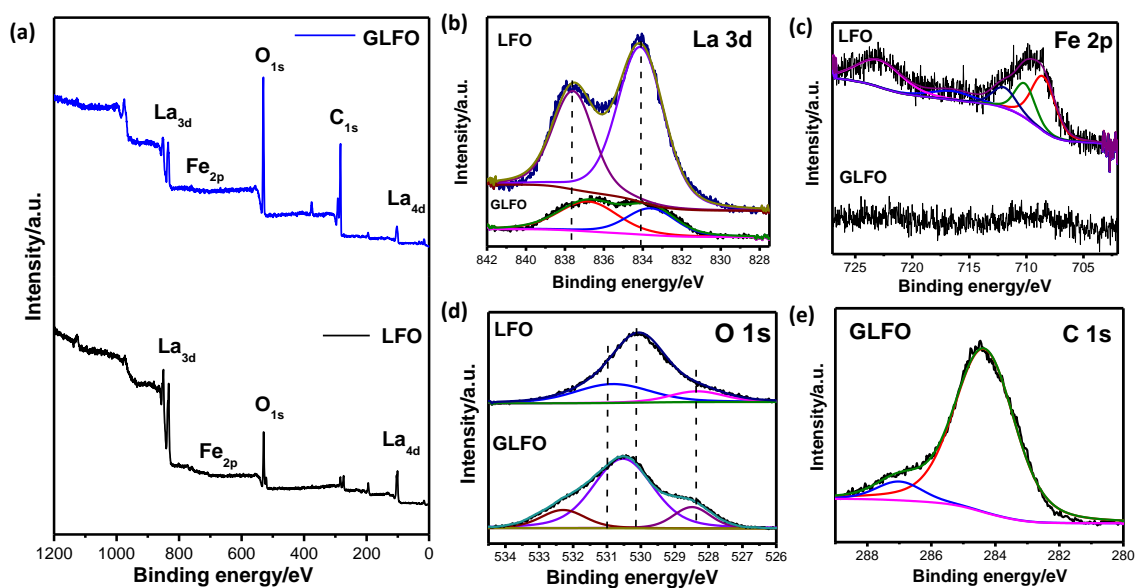
Fig. 3 – (a) Survey Spectra of LFO, GLFO, Core level XPS lineshape of (b) La 3d, (c) Fe 2p, (d) O 1s of bare LFO and GLFO (e) C 1s of GLFO.

The porous structure and the surface area of the LFO and GLFO nanocomposites have been studied by the nitrogen (N_2) adsorption-desorption isotherms (Fig. S2a and Fig. S2b). They show typical type-IV isothermals hysteresis loop suggests presence of mesoporous structures. The Brunauer–Emmett–Teller (BET) surface area of GLFO and LFO are 31 m² g^{-1} and 10 m² g^{-1} respectively which reveals that the nanocomposites show ~2.9 times larger surface area as compared to LFO. Moreover, the GLFO nanocomposites showed four-fold higher pore volume of 0.192 cm^3 g^{-1} in comparison to LFO with a pore volume of 0.048 cm^3 g^{-1} (Fig. S2a and Fig. S2b). This suggests that the incorporation of graphene rendered the nanocomposite with larger surface area and nanopores, which may improve the photocatalytic efficiency of the nanocomposites.

The chemical structures of the nanocomposites and the interactions between RGO and LFO have been further studied by FTIR analysis. The GLFO nanocomposites show characteristic

peaks at 3436, 1625, 1567, 1100, 637, 530 cm^{-1} (Fig. S3). The peaks at 3436 cm^{-1} of both LFO and GLFO nanocomposites correspond to O−H stretching vibration of the physisorbed water molecules. Peaks at 1636 cm^{-1} of LFO and 1625 cm^{-1} of GLFO nanocomposites are ascribed to the O−H bending vibration of the physisorbed water molecules [46]. In GLFO nanocomposites, the peak at 1567 cm^{-1} corresponds to the C=C stretching vibration of RGO. Peak at 1100 cm^{-1} arises due to the alkoxy C−O stretching vibration in the GLFO nanocomposites. Peak at 636 cm^{-1} of the GLFO and LFO nanocomposites respectively, correspond to the Fe−O stretching vibrations of the octahedral FeO$_6$ octahedra in LaFeO$_3$ [47]. Peaks at 530 and 541 cm^{-1} arise due to the La−O stretching vibration of the GLFO and LFO nanocomposites respectively. Thus, the vibration modes of both RGO and LFO are present in the FTIR spectra of GLFO, which is also evidence in favour of the successful formation of the nanocomposites.

3.4 Microstructures

Fig. 4a shows the formation of LFO nanorods of average length and width of ~331 nm and ~77 nm, respectively. The growth of LFO nanorods in the nanocomposites has been studied by varying the reaction time. At 24 h, growth of LFO nanorods have been started on the surface of the RGO (Fig. 4b) and complete formation of LFO nanorods with an average length and width of ~228 nm and ~64 nm, respectively was obtained at reaction time of 72 h (Fig. 4d).
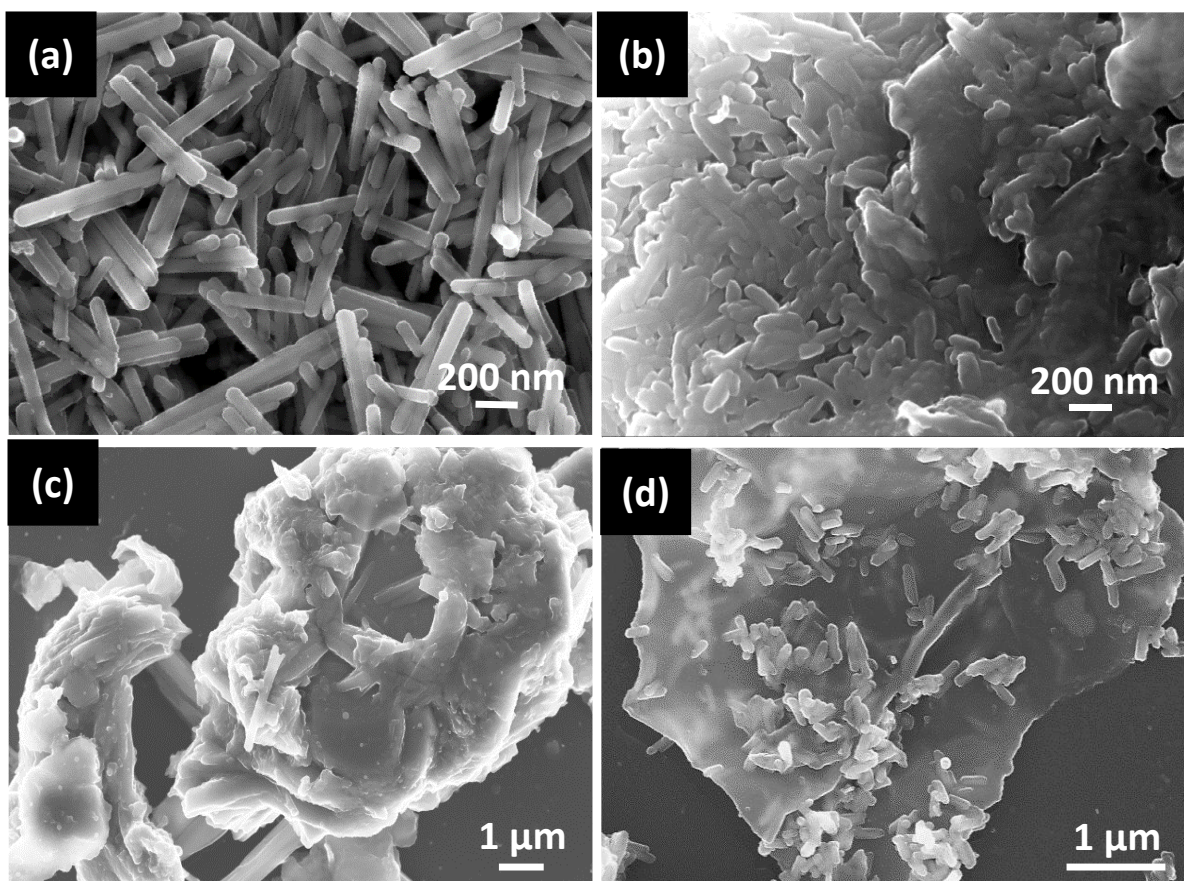
Fig. 4 – FESEM images of (a) bare LFO, (b) GLFO after hydrothermal treatment for 24 h, (c) GLFO after hydrothermal treatment for 48 h and (d) GLFO after hydrothermal treatment for 72 h.

Fig. 5 illustrates TEM and HRTEM images of the as-synthesized LFO and GLFO nanocomposites. The TEM images reveal that the uniform 1D structures of LFO are well consistent with the FESEM images. The TEM image of GLFO shows that LFO nanorods of average width ~77 nm are formed on the surface of RGO. The HRTEM images of GLFO exhibit clear lattice fringes and the interplanar spacing of 0.210 nm, 0.263 nm and 0.342 nm corresponds to the (212), (021) and (111) planes of orthorhombic LFO respectively (Fig. 5c). The SAED pattern (Fig. 5d) displays the diffraction rings, which correspond to the (332) and (221) planes of orthorhombic LaFeO$_3$.
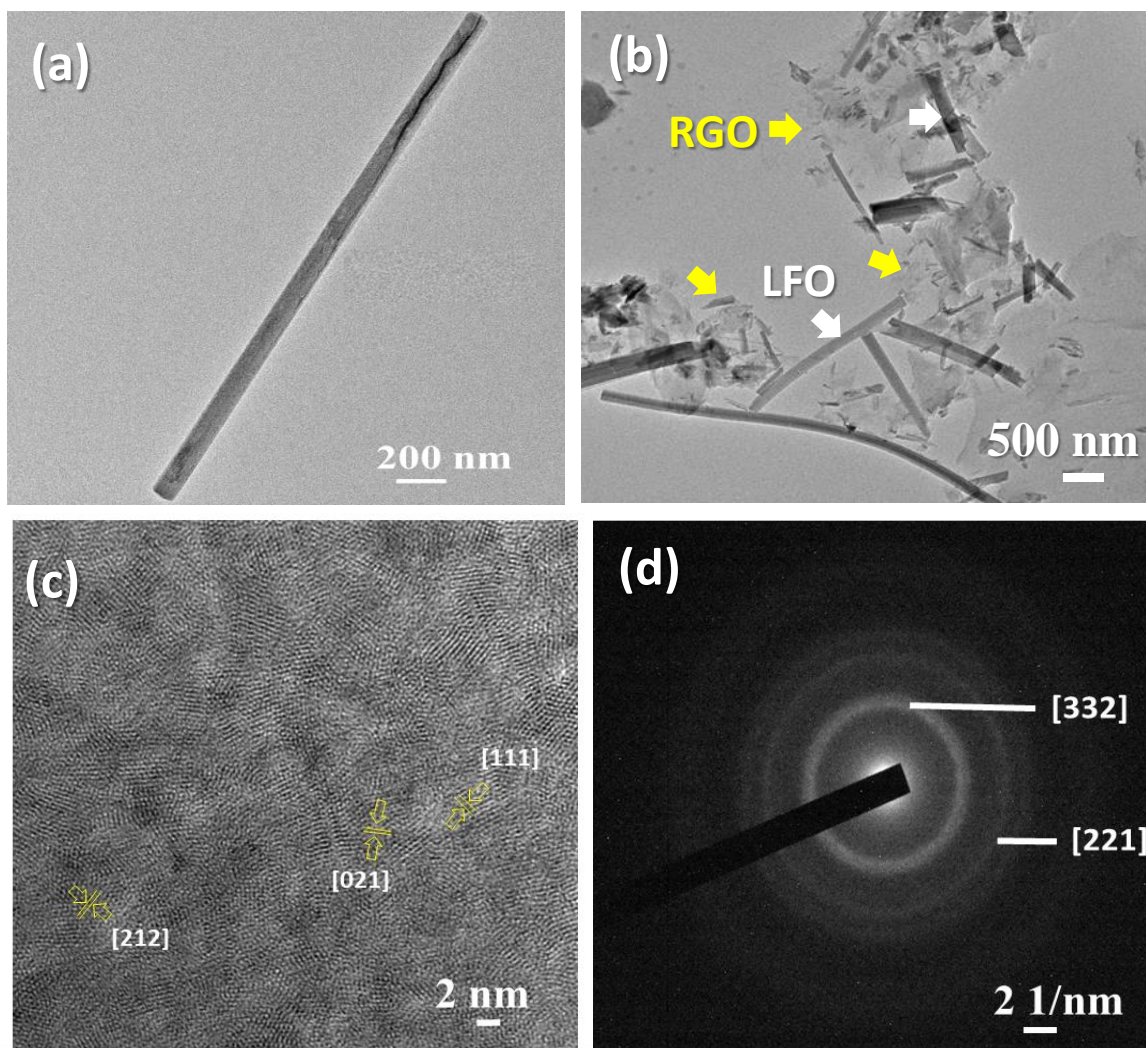
Fig. 5 – TEM images of (a) pure LFO, (b) GLFO, (c) HRTEM image of GLFO, (d) SAED Pattern of GLFO.

3.5 Thermal Properties

Thermogravimetric analysis (TGA) has been carried out to determine the thermal stability of the materials. A weight loss of 7% from 380-400°C has been observed for LFO, due to the removal of physiosorbed water molecules suggests superior thermal stability of metal oxides. For GLFO, a weight loss of 18% and a weight loss of 34% for RGO has been observed from 180-230°C due to pyrolysis of the labile oxygen-containing functional groups as shown in Fig. 6a [48]. In 240–500°C temperature range, the oxidative decomposition of carbon chains of

RGO was observed whereas, for GLFO nanocomposites, ~40 % mass loss was observed in the temperature range of 380-780°C, due to the decomposition of carbon chains of RGO [49]. It is important to note that for GLFO nanocomposites, the weight loss occurring due to the removal of oxygen-containing functionalities and the decomposition of carbon chains remarkably shifts towards higher temperatures as compared to RGO. This indicates the stability of the nanocomposites enhanced due to the presence of LFO.
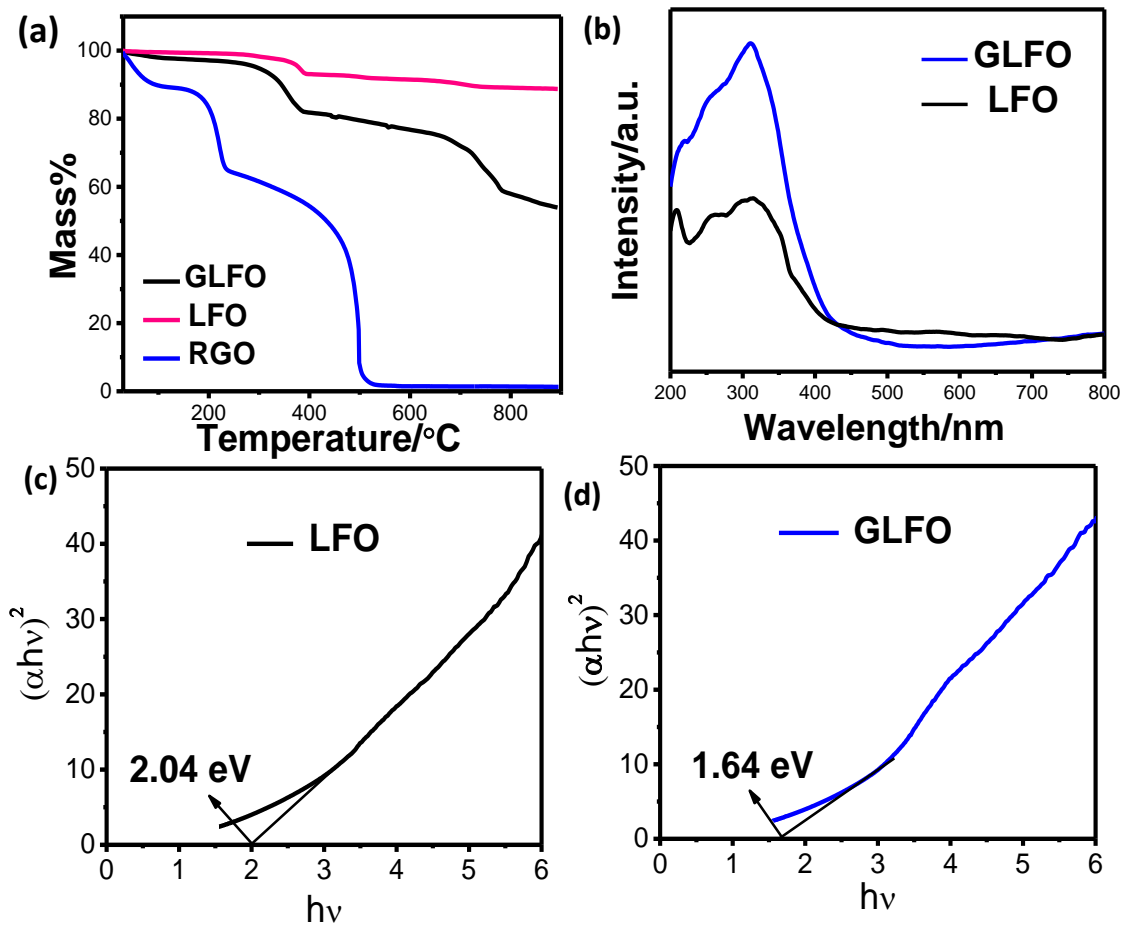

Fig. 6 − (a) TGA curves of LFO, GLFO nanocomposites. (b) UV-Visible Spectra of pure LFO and GLFO nanocomposites (c) KM plot of LFO (d) KM plot of GLFO nanocomposites.

3.6 UV-visible spectra

Fig. 6b illustrates the UV-visible diffuse reflectance spectra of LFO and GLFO nanocomposite where both show broad absorption in the visible region. The bandgap of LFO and GLFO nanocomposites are ~2.04 eV and ~1.64 eV, respectively calculated from the Kulbelka-Munk (KM) plots (Fig. 6c and Fig. 6d) [50]. This narrowing of bandgap after composite formation reveals that the composite may be capable of more visible light absorption as compared to pure $LaFeO_3$.

3.7 Photocatalytic hydrogen production

Fig. 7a shows photocatalytic H_2 generation by LFO and GLFO nanocomposites *via* water splitting in the presence of methanol solution. The rate of H_2 generation for LFO and GLFO nanocomposites are 9 mmol g^{-1} h^{-1} and 82 mmol g^{-1} h^{-1}, respectively. The nanocomposites show nine-fold enhancement in hydrogen generation as compared to pure LFO, which may be due to an enhancement of visible light absorption and more negative conduction band potential of GLFO as compared to LFO. Figure S4 shows the photocatalytic H_2 generation rate by GLFO nanocomposites synthesized for 24 hrs (GLFO-24), 48 hrs (GLFO-48) and 72 hrs (GLFO-72). This clearly reveals that the nanocomposites synthesized for 72 hrs shows the highest H_2 generation rate, which is almost ~1.9 times and 2.5 times higher than GLFO-48 and GLFO-24 respectively.

Different GLFO composites have also been prepared by varying the metal concentration and graphene concentration. The concentration of the metal precursors have been increased by 2.5 times (GLFO-2.5) and 5 times (GLFO-5) during the synthesis of the nanocomposites. From Fig. S7 we observe that the nanocomposites synthesized using the metal concentration, (0.002 M $La(NO_3)_3.6H_2O$ and 0.004 M $Fe(NO_3)_3.9H_2O$) shows the highest photocatalytic activity.

Figure S8 shows the photocatalytic H2 generation rate of GLFO nanocomposites using various concentration of graphene oxides such as 0.5 mg mL^{-1}, 1 mg mL^{-1}, 2 mg mL^{-1}. GLFO sample with 0.5 mg mL^{-1} loading of GO exhibits highest rate of photocatalytic H2 generation, as compared to the other two materials.

Table S1 shows the comparative study of LaFeO$_3$ based nanocomposites and graphene-based nanocomposites for photocatalytic applications [51−70]. Remarkably, as prepared 1D-2D based heterostructures of GLFO demonstrated superior photocatalytic activity for H$_2$ generation. Moreover, the photocatalyst showed no significant decrease of the catalytic activity and structural modification after several cycling test (Fig. S5).
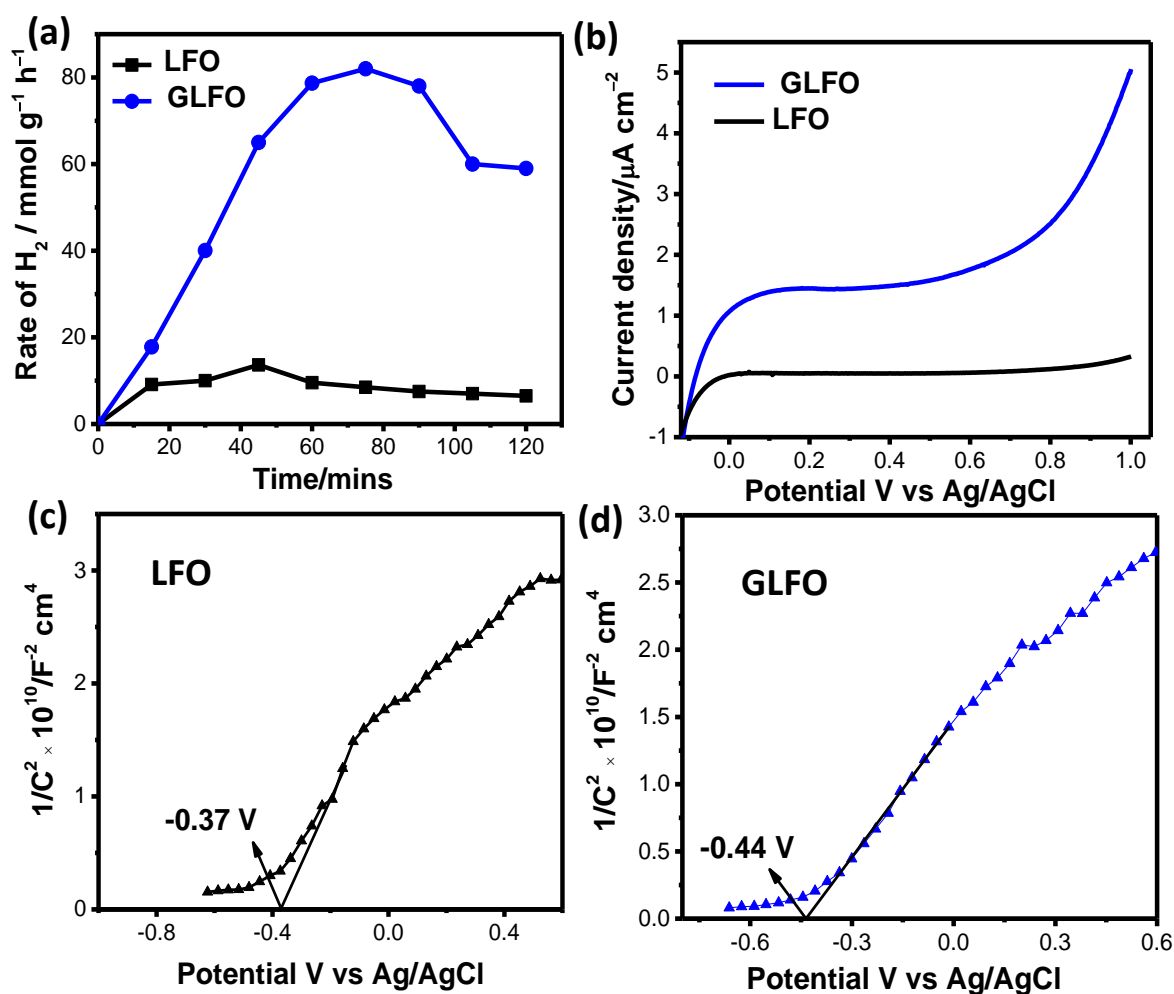
.

Fig. 7 − (a) Photocatalytic H₂ generation rate of LFO and GLFO nanocomposites. (b) LSV spectra of LFO and GLFO nanocomposites. Mott-Schottky plots of (c) LFO (d) GLFO.

3.8 Photoelectrochemical performance

Fig. 7b represents the linear sweep voltammetry (LSV) spectra of bare LFO and GLFO nanocomposites under light irradiation. GLFO nanocomposites and bare LFO exhibits a photocurrent density of 3.67 µA cm^{-2} and 0.17 µA cm^{-2} respectively at a potential of 0.9 V. Thus, the nanocomposites exhibit ~21 fold higher current density as compared to bare LFO. Furthermore, to check the photosensitivity, chronoamperometry of the as-prepared GLFO photoanode was checked under chopped light conditions, where a constant potential of 0.26 V was applied (Fig. S6). It has been clearly observed that the photoanode of GLFO is light-sensitive. The theoretical photoelectrochemical (PEC) H₂ generation for GLFO was calculated from the chronoamperometric spectra by determining the charge (Q) passed through the photoanode [25, 72]. The charge has been determined by integrating the current over the time and the moles of H₂ that is equal to $\frac{Q}{2F}$, where F is the Faraday constant (F = 96,500). The estimated PEC H₂ generation GLFO reaches to 0.7 µmol at 300 s. The Mott-Schottky (M-S) analysis have been carried out to understand the nature of semiconductors and flat band potentials (E$_{fb}$) [72-74]. Both the materials show positive slopes in M-S measurement thereby confirming n-type conductivity. Considering the difference between CB and E$_{fb}$ (ΔE), the conduction band minima (CBM) for both LFO and GLFO nanocomposites were calculated. The CBM potentials for LFO and GLFO nanocomposites are 0.04 eV and −0.03 eV, respectively (Fig. 7c and Fig. 7d). The more negative CBM of the nanocomposites boosts the efficiency of water reduction. The E$_g$ values can be determined from the Kubelka–Munk plots and the CBM values obtained from the Mott-Schottky analysis, the position of the VBM can

be calculated (Table 1). The VBM of bare LFO and GLFO nanocomposites are 2.08 eV and 1.61 eV respectively. The free charge carrier concentrations of GLFO nanocomposites (2.6×10^{17} cm^{-3}) is 1.3 times higher than that of LFO (1.9×10^{17} cm^{-3}). Hence, negative reduction potential with higher number of free charge carriers of GLFO may enhanced the photocatalytic performance of water splitting.

Table 1. Calculated Flat band potentials, CBM and VBM from the Mott-Schottky plots.

Material	**E$_{fb}$ vs Ag/AgCl (V)**	**E$_{fb}$ vs RHE (V)**	**CB (eV)**	**E$_g$ (eV)**	**VB (eV)**	**N$_d$ (cm^{-3})**
LFO	−0.37	0.24	0.04	2.04	2.08	1.9×10^{17}
GLFO	−0.44	0.17	−0.03	1.64	1.61	2.6×10^{17}

3.9 Mechanism

In order to further validates the energy diagrams calculated with the help of M-S and UV-Vis analysis, Secondary Electron Cut-off (SEC) spectra and valence band maxima (VBM) from XPS measurements was performed [75]. Fig. 8a represent the SEC spectra of GLFO and LFO. With the help of secondary electron cutoff energies, ionization potential (IP) and work function energies (φ) are determined, which are presented in Table 2. Clearly, both the IP and φ decrease after nanocomposites formation, which strongly reveals that coupling of RGO and LFO effectively create molecular bonding and dipole moments at the interface which further boosts the charge separation and reduce the overpotential to undergo the redox reactions at the surface. Furthermore, the VBM energies were determined from the valence band spectra of GLFO and LFO (Fig. 8b and Fig. 8c). A schematic band structure has been presented in Fig. 8d, which is

drawn, based on the values of VBM, work function and ionization potential energies to confirm the band edge potentials and the possible charge migration pathway.

Table 2. The secondary electron cutoff, work function energies, VBM position and ionization potential of the as developed materials.

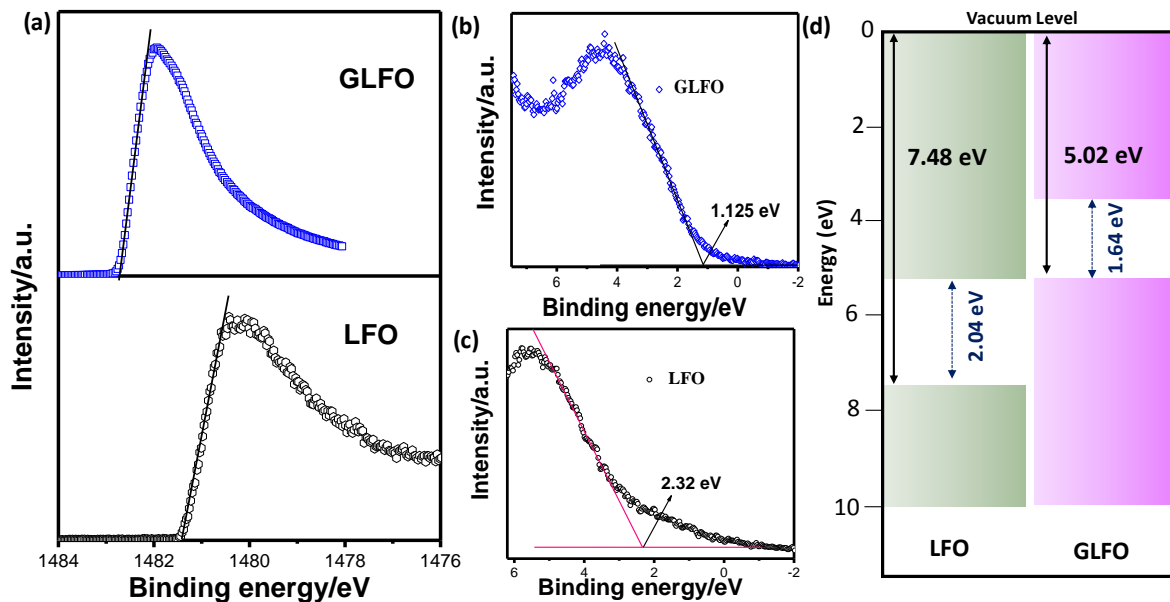| Material	SEC (eV)	φ (eV)	IP (eV)
LFO	1481.4	5.2	7.48
GLFO	1482.7	3.9	5.02

Fig. 8 – (a) SEC spectra of (a) GLFO and LFO, VB XPS of (b) GLFO and (c) LFO. (d) Schematic band structure of LFO and GLFO.

Fig. 9 demonstrates a plausible mechanism of the photocatalytic activity of GLFO nanocomposites. The charge migration occurs through the S-scheme heterojunction mechanism [76, 77]. RGO has higher CB and VB positions and lower work function compared to LFO. When the two semiconductors come in contact with each other, electrons in RGO

22

spontaneously migrate to LFO. This creates an electron depletion region and electron accumulation region near the interface in RGO and LFO, respectively. This leads to the formation of an internal electric field directing from RGO to LFO. This internal electric field accelerates the transfer of photogenerated electrons from LFO to RGO. When the two semiconductors come into contact, their Fermi energy should be aligned to the same level [78-80]. This causes an upward and downward bending of the Fermi levels of LFO and RGO, respectively which urges the recombination of the photogenerated electrons in the CB of LFO and holes in the VB of RGO at the interface region. The Coulombic attraction between holes and electrons assists the recombination of the photogenerated electrons in the CB of LFO and holes in the VB of RGO at the interface. The photogenerated electrons which are reserved in the CB of RGO and photogenerated holes present in the VB of LFO may perform the reduction and oxidation reactions respectively.
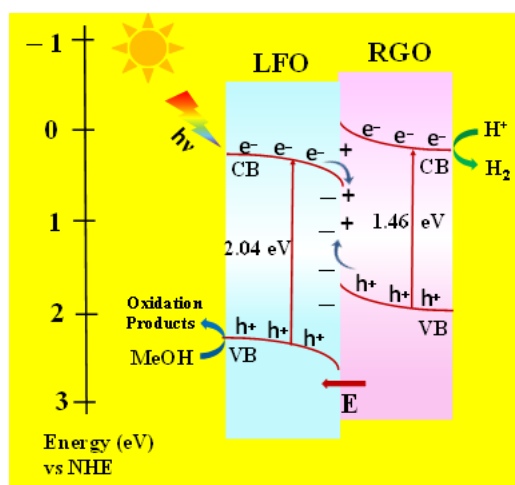

Fig. 9 – Charge-transfer mechanism of the GLFO nanocomposites.

4. CONCLUSION

A stable LaFeO$_3$/Reduced Graphene Oxide nanocomposites have been synthesized by hydrothermal method for visible light driven photocatalytic application. A nine-fold enhancement in the rate of photocatalytic H$_2$ generation has been achieved for the

nanocomposites as compared to bare $LaFeO_3$. The nanocomposites formation significantly enhances the photoelectrochemical current density (~21 times) under visible light irradiation. Improved photocatalytic performance of LFO the presence of RGO nanocomposites showed superior photocatalytic activity in water reduction due to the more negative CB potential, greater number of free charge carriers, lower ionization potential and exceptional ability of the RGO to promote charge transport. Incorporation of RGO nanosheets to $LaFeO_3$ lowered the bandgap of the nanocomposites, thereby causing an enhancement in visible light absorption as well as provided much better charge separation. Thus, the $LaFeO_3$/ RGO nanocomposites reveal to be an effective visible light active photocatalyst and can be extended to other photocatalytic applications such as pollution control or CO_2 conversion to useful hydrocarbon products and fuels.

CONFLICT OF INTEREST

The authors have declared no conflicts of interest for this article.

REFERENCES

(1) Al-Shetwi AQ. Sustainable development of renewable energy integrated power sector: Trends, environmental impacts, and recent challenges. Sci Total Environ 2022; 822: 153645.

(2) Li H, Wang H, Li X, Huang J, Kheng S, Hiang B, Lee K, Hana J, Guoa R. Boosting solar-to-pyroelectric energy harvesting via a plasmon-enhanced solar-thermal conversion approach. Nano Energy 2022; 100:107527.

(3) Yadav RK, Lee JO, Kumar A, Park NJ, Yadav D, Kim JY, Baeg, JO. Highly Improved Solar Energy Harvesting for Fuel Production from CO_2 by a Newly Designed Graphene Film Photocatalyst. Sci Rep 2018; 8:16741−51.

(4) Nevárez MC, Onu M, Lukasz C, Haliński P, Miodyńsk M, Parnick P, Bajorowicz B, Kobylański M, Lewandowski L, Zaleska-Medynska A. Hydrogen detection during photocatalytic water splitting: A tutorial. Int J Hydrog Energy 2022; 47:15783−88.

(5) Kovacic Z, Likozar B, Hus M. Photocatalytic CO_2 Reduction: A Review of Ab Initio Mechanism, Kinetics, and Multiscale Modelling Simulations. ACS Catal 2020; 10:14984−15007.

(6) Hisatomi T, Domen K. Reaction systems for solar hydrogen production via water splitting with particulate semiconductor photocatalysts. Nat Catal 2019; 2:387−399.

(7) Fujishima A, Honda K. Electrochemical Photolysis of Water at a Semiconductor Electrode. Nature 1972; 238:37.

(8) Nakata K, Fujishima A. TiO_2 photocatalysis: Design and applications, Journal of Photochemistry and Photobiology C: Photochemistry Reviews. J Photochem Photobiol C 2012; 13:169−89.

(9) Leong S, Razmjou A, Wang K, Hapgood K, Zhang X, Wang H. TiO_2 based photocatalytic membranes: A review. J Membr Sci 2014; 472:167−84.

(10) Dong H, Zeng G, Tang L, Fan C, Zhang C, He X, He Y. An overview on limitations of TiO_2-based particles for photocatalytic degradation of organic pollutants and the corresponding countermeasures. Water Res 2015; 79:128–46.

(11) Chavali MS, Nikolova MP. Metal oxide nanoparticles and their applications in nanotechnology. SN Appl Sci 2019; 1:607–37.

(12) Teh YW, Chee MKT, Kong XY, Yong ST, Chai SP. An insight into perovskite-based photocatalysts for artificial photosynthesis. Sustain Energy Fuels 2020; 4:973–84.

(13) Irshad M, Ain Q, Zaman M, Aslam MZ, Kousar N, Muhammad A, Rafique M, Siraj K, Tabish AN, Usman M, Farooq MH, Assiri MA, Imran M. Photocatalysis and perovskite oxide-based materials: a remedy for a clean and sustainable future. RSC Adv 2022; 122:7009–39.

(14) Kumar A, Kumar A, Krishnan V. Perovskite Oxide Based Materials for Energy and Environment-Oriented Photocatalysis. ACS Catal 2020; 10:10253–315.

(15) Dandia A, Saini P, Sharma R, Parewa V. Visible light driven perovskite-based photocatalysts: A new candidate for green organic synthesis by photochemical protocol. Curr Res Green Sustain Chem 2020; 3:100031–91.

(16) Khan LY, Mohtar SS, Aziz F. Floatable photocatalyst $LaFeO_3$/modified expanded perlite composite for photocatalytic ammonia degradation. J Water Process Eng 2021; 44:102401.

(17) Humayun M, Ullah H, Usman M, Habibi-Yangjeh A, Tahir AA, Wang C, Luo W. Perovskite-type lanthanum ferrite based photocatalysts: Preparation, properties, and applications. J Energy Chem 2022; 66:314–38.

(18) Wang Q, Guan S, Li B. 2D graphitic-C_3N_4 hybridized with 1D flux-grown Na-modified $K_2Ti_6O_{13}$ nanobelts for enhanced simulated sunlight and visible-light photocatalytic performance. Catal Sci Technol 2017; 7:4064–78.

(19) Meng F, Li J, Cushing SK, Zhi M, Wu N. Solar Hydrogen Generation by Nanoscale p–n Junction of p-type Molybdenum Disulfide/n-type Nitrogen-Doped Reduced Graphene Oxide. J Am Chem Soc 2013; 135:10286−89.

(20) Wang J, Tang L, Zeng G, Deng Y, Dong H, Liu Y, Chen F. 0D/2D interface engineering of carbon quantum dots modified Bi_2WO_6 ultrathin nanosheets with enhanced photoactivity for full spectrum light utilization and mechanism insight. Appl Catal B: Environ 2018; 222:115−23.

(21) Bera S, Kumari A, Ghosh S, Basu RN. Assemble of Bi-doped TiO_2 onto 2D MoS_2: an efficient p–n heterojunction for photocatalytic H_2 generation under visible light. Nanotechnology 2021; 32:195402–414.

(22) He Z, Zhang, J, Li X, Guan S, Dai M, Wang S. 1D/2D Heterostructured Photocatalysts: From Design and Unique Properties to Their Environmental Applications. Small 2020; 16:2005051−68.

(23) Qian HZ, Wang B, Liu MT, Zhao NN, Wang ZH, Peng Y. Unique 1D/2D $Bi_2O_2CO_3$ nanorod-Bi_2WO_6 nanosheet heterostructure: synthesis and photocatalytic performance. Cryst Eng Comm 2021; 23:6128–36.

(24) Liang Q, Gao W, Liu C, Xu S, Li Z. A novel 2D/1D core-shell heterostructures coupling MOF-derived iron oxides with $ZnIn_2S_4$ for enhanced photocatalytic activity. J Hazard Mater 2020; 392:122500−12.

(25) Bera S, Ghosh S, Maiyalagan T, Basu RN. Band Edge Engineering of $BiOX/CuFe_2O_4$ Heterostructures for Efficient Water Splitting. ACS Appl Energy Mater 2022; 5:3821−33.

(26) Bera S, Ghosh S, Basu RN. Silver as solid-state electron mediator in $MoS_2/Ag−AgVO_3$ Z-Scheme heterostructures for photocatalytic H_2 generation. J Alloys Compd 2020; 830:154527−39.

(27) Wang J, Wang Z, Qu P, Xu Q, Zheng J, Jia S, Chen J. A 2D/1D TiO$_2$ nanosheet/CdS nanorods heterostructure with enhanced photocatalytic water splitting performance for H$_2$ evolution. Int J Hydrog Energy 2018; 43:7388–96.

(28) Ullah K, Zhu L, Meng ZD, Ye S, Sarkar S, Oh WC. Synthesis and characterization of novel PtSe$_2$/graphene nanocomposites and its visible light driven catalytic properties. Mater Sci Semicond Proc 2014; 25:301–306.

(29) Al-Rawashdeh AF, Allabadi O, Aljarrah MT. Photocatalytic Activity of Graphene Oxide/Zinc Oxide Nanocomposites with Embedded Metal Nanoparticles for the Degradation of Organic Dyes. ACS Omega 2020; 43:28046–55.

(30) Bramhaiah K, Bhattacharyya S. Challenges and future prospects of graphene-based hybrids for solar fuel generation: moving towards next generation photocatalysts. Mater Adv 2022; 3:142–72.

(31) Dang H, Dong X, Dong Y, Huang, J. Facile and green synthesis of titanate nanotube/graphene nanocomposites for photocatalytic H$_2$ generation from water. Int. J. Hydrog. Energy 2013; 38:9178–9185.

(32) Alsulami QA, Rajeh A, Baamer DF. Preparation of highly efficient sunlight driven photodegradation of some organic pollutants and H$_2$ evolution over rGO/FeVO$_4$ nanocomposites. Int. J. Hydrog. Energy 2021; 46:27349–27363.

(33) Hafeez HY, Lakhera SK, Neppolian B. Synergetic improvement in charge carrier transport and light harvesting over ternary InVO$_4$-g-C$_3$N$_4$/rGO hybrid nanocomposite for hydrogen evolution reaction. Int J Energy Res 2020; 45:7530–7540.

(34) Acharya S, Padhi DK, Parida KM. Visible light driven LaFeO$_3$ nano sphere/RGO composite photocatalysts for efficient water decomposition reaction. Catal Today 2020; 353:220–31.

(35) Orak C, Yüksel A. Graphene- supported $LaFeO_3$ for photocatalytic hydrogen energy production. Int J Energy Res 2021; 45:12898–914.

(36) Yu H, Zhang B, Bulin C, Li R, Xing R. High-efficient Synthesis of Graphene Oxide Based on Improved Hummers Method. Sci Rep 2016; 6:36143−50.

(37) Stobinski L, Lesiak B, Malolepszy A, Mazurkiewicz M, Mierzwa B, Zemek J, Jiricek P, Bieloshapka I. Graphene oxide and reduced graphene oxide studied by the XRD, TEM and electron spectroscopy methods. J Electron Spectros Relat Phenomena 2014;195: 145−54.

(38) PapageorgiouIan DG, Robert AK, Young J. Graphene/elastomer nanocomposites. Carbon 2015; 95:460−84.

(39) Weber MC, Guennou M, Zhao HJ, Íñiguez J, Vilarinho R, Almeida A, Kreisel J. Raman spectroscopy of rare-earth orthoferrites $RFeO_3$ (R=La, Sm, Eu, Gd, Tb, Dy). Phys Rev B 2016; 94:214103−11.

(40) Orlando A, Franceschini F, Muscas C, Pidkova S, Bartoli M, Rovere M, Tagliaferro A. A Comprehensive Review on Raman Spectroscopy Applications. Chemosensors 2021;9: 262−90.

(41) Beams R, Cançado LG, Novotny L. Raman characterization of defects and dopants in graphene. J Phys Condens Matter 2015; 27:083002−29.

(42) Muzyka R, Drewniak S, Pustelny T, Chrubasik M, Gryglewicz G. Characterization of Graphite Oxide and Reduced Graphene Oxide Obtained from Different Graphite Precursors and Oxidized by Different Methods Using Raman Spectroscopy. Materials 2018; 11:1050−65.

(43) Minitha CR, Rajendrakumar RT. Synthesis and Characterization of Reduced Graphene Oxide. Adv Mater Res 2013; 678:56−60.

(44) Vijayaraghavan T, Sivasubramanian R, Hussain S, Ashok A. A Facile Synthesis of LaFeO$_3$-Based Perovskites and Their Application towards Sensing of Neurotransmitters. Chemistry Select 2017; 2:5570–77.

(45) Rella S, Giuri A, Esposito C, Rosaria CM, Acocella MR, Colella S, Guerra G, Listorti A, Rizzo A, Malitesta C. X-ray photoelectron spectroscopy of reduced graphene oxide prepared by a novel green method. Vacuum 2015; 119:159–62.

(46) Andrijanto E, Shoelarta S, Subiyanto G, Rifki S. Facile synthesis of graphene from graphite using ascorbic acid as reducing agent. AIP Conf Proc 2016; 1725:020003–8.

(47) Sharma N, Kushwaha HS, Sharma SK, Sachdev K. Fabrication of LaFeO$_3$ and rGO-LaFeO$_3$ microspheres based gas sensors for detection of NO$_2$ and CO. RSC Adv 2020; 10: 1297–1308.

(48) Ghosh S, Holade Y, Remita, H, Servat K, Beaunier P, Hagege A, Kokoh KB, Napporn, TW. One-pot synthesis of reduced graphene oxide supported gold-based nanomaterials as robust nanocatalysts for glucose electrooxidation. Electrochim Acta 2016; 212:864–75.

(49) Mukherjee A, Chakrabarty S, Kumari N, Su WN, Basu S. Visible-Light-Mediated Electrocatalytic Activity in Reduced Graphene Oxide-Supported Bismuth Ferrite. ACS Omega 2018; 3:5946−57.

(50) Kubelka P, Munk F. An article on optics of paint layers. Z Tech Phys 1931; 12:593–601.

(51) Acharya S, Mansingh S, Parida KM. The enhanced photocatalytic activity of g-C$_3$N$_4$-LaFeO$_3$ for the water reduction reaction through a mediator free Z-scheme mechanism. Inorg Chem Front 2017; 4:1022–32.

(52) Xu K, Feng J. Superior photocatalytic performance of LaFeO$_3$/g-C$_3$N$_4$ heterojunction nanocomposites under visible light irradiation. RSC Adv 2017; 7:45369−76.

(53) Xu K, Xu H, Feng G, Feng J. Photocatalytic hydrogen evolution performance of NiS cocatalyst modified LaFeO$_3$/g-C$_3$N$_4$ heterojunctions. New J Chem 2017; 41:14602–9.

(54) Ismael M, Wu Y. Facile synthesis method for fabrication of LaFeO$_3$/g-C$_3$N$_4$ nanocomposite as efficient visible-light-driven photocatalyst for photodegradation of RhB and 4-CP. New J Chem 2019;43 :13783−93.

(55) Das S, Dutta S, Tama AM, Basith MA. Nanostructured LaFeO$_3$-MoS$_2$ for efficient photodegradation and photocatalytic hydrogen evolution. Mater Sci Eng 2021; 271:115295.

(56) Saleh R, Hidayat SA, Rizal MY, Taufik A, Yin S. Synthesis and characterization of BiFeO$_3$/LaFeO$_3$/graphene composites as persulfate activator for removal of 4-nitrophenol. Adv Powder Technol 2022; 33:103752.

(57) Wu H, Hu R, Zhou T, Li C, Meng W, Yang J. A novel efficient boron-doped LaFeO$_3$ photocatalyst with large specific surface area for phenol degradation under simulated sunlight. Cryst Eng Comm 2015; 17:3859−65.

(58) Xu C, Jin Z, Yang J, Guo F, Wang P, Meng H, Bao G, Li Z, Chen C, Liu F, Hu R. A direct Z-scheme LaFeO$_3$/WO$_3$ photocatalyst for enhanced degradation of phenol under visible light irradiation. J Environ Chem Eng 2021; 9:106337.

(59) Pirzada BM, Pushpendra, Kunchala RK, Naidu BS. Synthesis of LaFeO$_3$/Ag$_2$CO$_3$ Nanocomposites for Photocatalytic Degradation of Rhodamine B and p-Chlorophenol under Natural Sunlight. ACS Omega 2019; 4:2618–29.

(60) Lu Y, Ma B, Yang Y, Huang E, Ge Z, Zhang T, Zhang S, Li L, Guan N, Ma Y, Chen Y. High activity of hot electrons from bulk 3D graphene materials for efficient photocatalytic hydrogen production. Nano Res. 2017; 10:1662−72.

(61) Sethi YA, Kulkarni AK, Ambalkar A, Panmand RP, Kulkarni MV, Gosavi SW, Kale B. Enhanced Photocatalytic Remediation Using Graphene (G)-Titanium Oxide (TiO$_2$) Nanocomposite Material in Visible Light Radiation. Chem Soc Rev 2012; 41:782–96.

(62) Rabiatul N, Shah AM, Mohamad RY, Nurul Y, Wai NR, Khuzaimah YW, Lorna A, Minggu J. Current progress on 3D graphene-based photocatalysts: From synthesis to photocatalytic hydrogen production. Int J Hydrog Energy 2021; 46:9324–40.

(63) Zhang J, Yu J, Jaroniec M, Gong JR. Noble Metal-Free Reduced Graphene Oxide-$Zn_xCd_{1-x}S$ Nanocomposite with Enhanced Solar Photocatalytic H_2-Production Performance. Nano Lett 2012; 12:4584–89.

(64) Strotman NA, Baxter CA, Brands KMJ, Cleator E, Krska SW, Reamer RA, Wallace DJ, Wright TJ. Highly Efficient Visible-Light-Driven Photocatalytic Hydrogen Production of CdS-Cluster-Decorated Graphene Nanosheets. J Am Chem Soc 2011; 133:10878−84.

(65) Ding J, Yan W, Xie W, Sun S, Bao J, Gao C. Highly efficient photocatalytic hydrogen evolution of graphene/$YInO_3$ nanocomposites under visible light irradiation. Nanoscale 2014; 6:2299–307.

(66) He F, Meng A, Cheng B, Ho W. Enhanced photocatalytic H_2-production activity of WO_3/TiO_2 step-scheme heterojunction by graphene modification. Chinese J Catal 2020; 41:9–20.

(67) Wang M, Ju P, Li J, Zhao Y, Han X, Hao Z. Facile Synthesis of MoS_2/g- C_3N_4/GO Ternary Heterojunction with Enhanced Photocatalytic Activity for Water Splitting. ACS Sustain Chem Eng 2017; 5:7878−86.

(68) Zhao W, Zhang Z, Zhang J, Wu H, Xi L, Ruan C. Microwave-assisted synthesis of Ag–TiO_2/graphene composite for hydrogen production under visible light irradiation. Ceram Int 2016; 42:18257–63.

(69) Azam MU, Tahir M, Siraj M. In-situ synthesis of TiO_2/$La_2O_2CO_3$/rGO composite under acidic/basic treatment with La^{3+}/Ti^{3+} as mediators for boosting photocatalytic H_2 evolution. Int. J. Hydrog. Energy 2019; 44:23669–23688.

(70) Muninathan S, Arumugam S. Enhanced photocatalytic activities of NiS decorated reduced graphene oxide for hydrogen production and toxic dye degradation under visible light irradiation. Int. J. Hydrog. Energy 2021; 46:6532–6546.

(71) Morales-Guio CG, Tilley SD, Vrubel H, Grätzel M, Hu X. Hydrogen evolution from a copper(I) oxide photocathode coated with an amorphous molybdenum sulphide catalyst. Nat Commun 2014; 5:3059–3066.

(72) Sivula K. Mott–Schottky Analysis of Photoelectrodes: Sanity Checks Are Needed. ACS Energy Lett 2021; 6:2549–51.

(73) Liu Y, Guo J, Zhu E, Liao L, Lee SJ, Ding M, Shakir I, Gambin V, Huang Y, Duan X. Approaching the Schottky-Mott limit in van der Waals metal-semiconductor junctions. Nature 2018; 557:696–700.

(74) Matsumoto, Y. Energy Positions of Oxide Semiconductors and Photocatalysis with Iron Complex Oxides. J Solid State Chem 1996; 126:227–34.

(75) Greczynski G, Hultman L. X-ray photoelectron spectroscopy: Towards reliable binding energy referencing. Prog Mater Sci 2020; 107:100591–637.

(76) Zhang L, Zhang J, Yu H, Yu J. Emerging S-Scheme Photocatalyst. Adv. Mater 2021; 34: 2107668–84.

(77) Xu Q, Wageh S, Al-Ghamdi AA, Li X. Design principle of S-scheme heterojunction photocatalyst. J Mater Sci Technol 2022; 124: 171–173.

(78) Sharmin F, Roy DC, Basith MA. Photocatalytic water splitting ability of Fe/MgO-rGO nanocomposites towards hydrogen evolution Int. J. Hydrog. Energy 2021; 46: 38232–38246.

(79) Kuang P, Sayed, M, Fan J, Cheng B, Yu J. 3D Graphene- Based H_2 - Production Photocatalyst and Electrocatalyst. Adv. Energy Mater. 2020; 10: 1903802–1903855.

(80) Boppella R, Choi CH, Moon J, Ha Kim, D. Spatial charge separation on strongly coupled 2D-hybrid of rGO/La$_2$Ti$_2$O$_7$ /NiFe-LDH heterostructures for highly efficient noble metal free photocatalytic hydrogen generation. Appl. Catal. B: Environ., 2018; 239: 178–186.